Orbital Filter Aiding of a High Sensitivity GPS Receiver for Lunar Missions

VINCENZO CAPUANO, PAUL BLUNT, CYRIL BOTTERON and PIERRE-ANDRÉ FARINE

ESPLAB, École Polytechnique Fédérale de Lausanne (EPFL)

Received March 2016; Revised January 2017

ABSTRACT: *Recent studies have shown that weak global navigation satellite system (GNSS) signals could potentially be used to navigate from Earth to the Moon. This would increase autonomy, robustness, and flexibility of the navigation architectures for future lunar missions. However, the utilization of GNSS signals at very high altitudes close to the Moon can be significantly limited by the very low power levels seen at the receiver's antenna. This can result in a strongly reduced visibility of the GNSS satellites, which can worsen the already poor relative geometry of the GNSS receiver to the GNSS satellites. Furthermore, during most of a Moon transfer orbit (MTO), the very weak GNSS signals are also affected by Doppler shifts and Doppler rates larger than the ones generally experienced on Earth, due to the much higher relative dynamics between the receiver and the transmitters. As a consequence, commercial GNSS receivers for terrestrial use cannot successfully acquire and track such signals. More advanced architectures and specific implementations are thus required to use GNSS for lunar missions. In this paper, we propose the use of an adaptive orbital filter to aid the GNSS acquisition and tracking modules and to strongly increase the achievable navigation accuracy. The paper describes the orbital filter architecture and tests results carried out by processing realistic radio frequency (RF) signals generated by our Spirent GSS 8000 full constellation simulator for a highly elliptical MTO.*

INTRODUCTION

Several studies such as [1–4] have shown the efficiency of using an orbital forces model to filter GNSS measurements for space navigation. Other studies such as [5, 6] have proved the feasibility of acquiring and tracking GNSS signals up to the Moon altitude, even if these signals are weak and affected by Doppler shifts and Doppler rates significantly higher than on Earth. The solution we discuss in this paper is based on the filtering of GPS observations through an orbital forces model, which propagates the kinematic state of the spacecraft on the way to the Moon. The GPS measurements prevent the orbital propagation solution from drifting, while the orbital propagation smooths the GPS solution and bridges signal outages.

The resultant architecture, basically a GPS-based orbital filter, is first used to mitigate the effect of the very high GDOP and large ranging errors, and then to aid the GPS receiver to acquire and track the weak GPS signals also in high dynamic conditions.

Figure 1 illustrates a basic block diagram of the research milestones we have reached in the past three years, with the aim of developing a GNSS-based navigation system for lunar missions. For the first milestone, we have investigated the characteristics of the GNSS signals and analyzed the feasibility of using them for a Moon mission; this has been described in [6]. The achievement of this milestone provided all the requirements to design and then develop a GNSS signal processing engine as a proof of concept for lunar missions, which is the second achieved milestone, described in [7]. However, the navigation performance achievable by using only unfiltered GNSS receiver observations is very coarse, and only a few signals can be tracked and decoded. Following this, for the same mission, we have implemented a GNSS-based orbital filter, which is the third milestone, described in detail in [4], with a significant improvement of the navigation accuracy. Finally, we focused on using the aiding that the orbital filter can provide to the GNSS receiver, in order to make it capable of acquiring and tracking a larger number of GNSS signals at

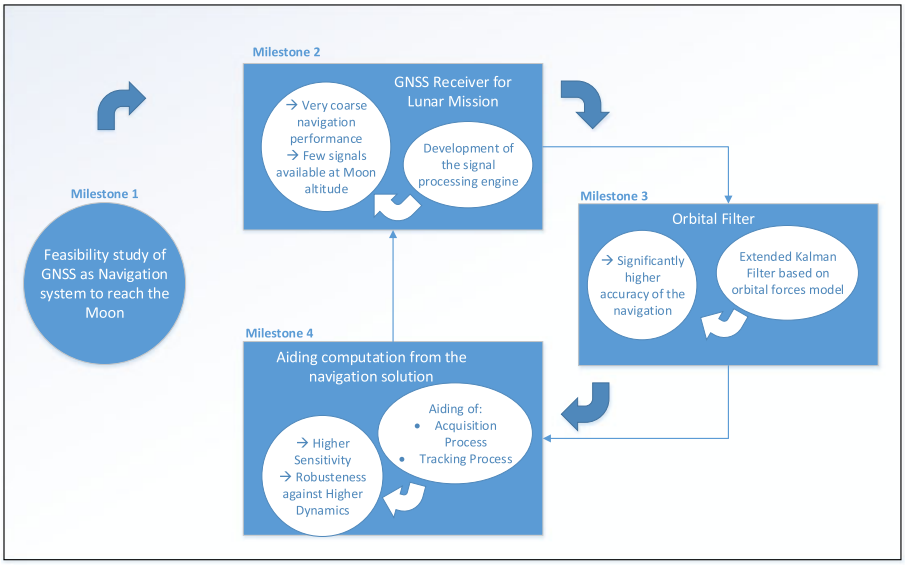

Fig. 1–Basic block diagram of our research in GNSS for lunar missions. [Color figure can be viewed at wileyonlinelibrary.com and www.ion.org]

the Moon altitude. This is the fourth milestone and is the topic of this paper. Note that as illustrated by the thinner lines in Figure 1, the GNSS receiver, the orbital filter, and the aiding computation are not only milestones but also subsystems of the full architecture and part of a closed loop system. The GNSS receiver provides GNSS observations, which are passed to the orbital filter to be filtered and transformed to position and velocity of the receiver, and these later are then manipulated to be used as aiding for the signal processing.

More specifically, the aiding block estimates carrier frequency and Doppler rate, computed from the integrated navigation solution, and provides them as assistance to the acquisition engine, reducing the number of cells to be searched to acquire the signal and enabling longer integration times, and therefore, the acquisition of weaker signals. The same assistance is provided to the tracking loops in such a way that they only have to track the receiver clock noise and the error of the integrated navigation solution, instead of the absolute dynamics of the user antenna. This increases noise resistance and tracking sensitivity.

The rest of this paper is organized as follows. In the Mission Scenario Description section, we describe the mission scenario; we report the MTO trajectory parameters and provide a summary of the GPS L1 C/A characteristics for the considered trajectory. The section on The WeakHEO Receiver contains a brief description of the "*WeakHEO*" receiver, a GPS L1 receiver proof of concept, above-mentioned, developed in our lab, specifically for lunar missions. In The Orbital Filter section, we describe the design and implementation of our GPS-based orbital filter for lunar missions, which is based on an adaptive extended Kalman filter (EKF). The Navigation Performance section outlines the achieved navigation performance in terms of position, velocity, and Doppler estimation accuracy, after first providing a description of the simulation models, simulation results for the full MTO, and hardware-in-the-loop (HIL) test results for a portion of the full MTO. Finally, the Orbital Filter Aiding to the GNSS Module section provides a detailed description of the orbital filter aiding to the GNSS modules.

MISSION SCENARIO DESCRIPTION

Reference Trajectory

Although indirect ways of reaching the Moon exist, in this study as in [7], we have considered a simple direct MTO as reference kinematics of the GPS receiver. This trajectory corresponds to the light blue portion of Earth to the Moon trajectory illustrated in Figure 2. The considered MTO is defined by the initial kinematic state and the spacecraft parameters presented in Table 1. The full reference trajectory of the considered MTO has been validated using the much more accurate orbital propagator (HPOP) of the STK, which, unlike the one used by the orbital filter (to predict the GNSS observations), includes perturbations such as Earth gravitational potential spherical harmonics up to the 21st order and 21st degree, tidal forces, atmospheric drag, solar radiation pressure, and gravitational third-body perturbation due to both the Moon and the Sun [8]. The divergence between the trajectories generated under the orbital forces model used for the reference and the one used for

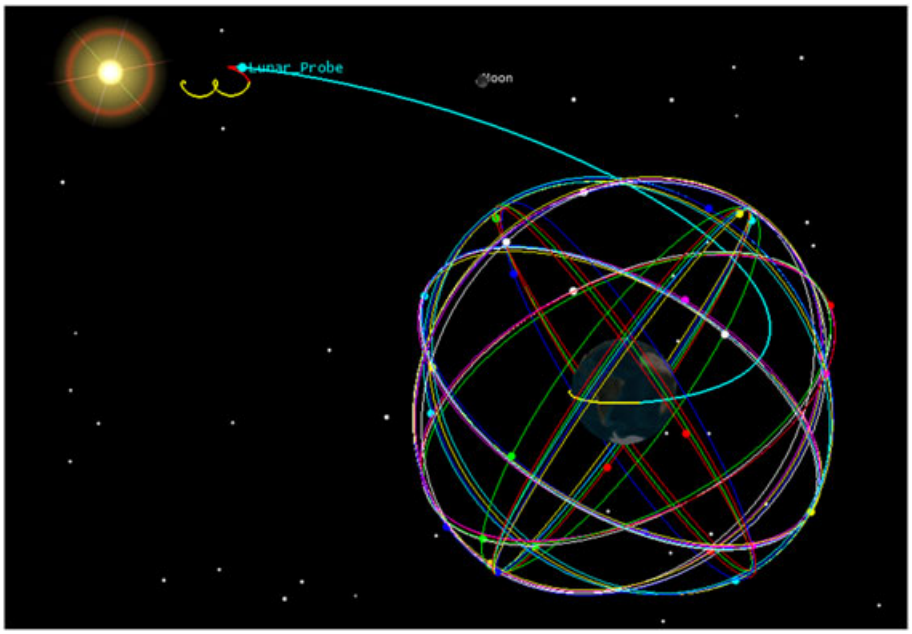

Fig. 2–Considered lunar mission: the MTO is the curve in light blue (image generated by using STK). [Color figure can be viewed at wileyonlinelibrary.com and www.ion.org]

Table 1—Initial Kinematic State and Parameters of the Spacecraft

Parameters	Values
ECI initial position (km)	[2395.52, −5298.28, −3022.82]
ECI initial velocity (km/s)	[10.19, 3.58, 1.72]
Departure date	July, 2 2005, 00:34:18
Mass of the spacecraft (kg)	1000
Reference surface (m^2)	20
Radiation pressure coefficient	1

the estimator in the orbital filter reaches almost 300 km at the end of MTO, as shown in Figure 7 of our previous work [3].

GPS Signal Characteristics

Our previous studies [6, 7, 9] have explored the GPS L1 C/A signal characteristics in detail during the considered MTO. These studies assumed that all signals in the considered GPS antenna sidelobes can be used for navigation as demonstrated with in-orbit measurements in [10]. The results shown in Figure 3, which shows the same results obtained in Figure 5 of [7], have revealed that, by assuming a 0-dBi receiver antenna gain, the fourth strongest GPS L1 C/A signal (at least four ranges are required to compute the 3D position) at receiver antenna never goes below a power level of −168.5 dBm, neglecting a few lower peaks. Therefore, a very high sensitivity receiver architecture is required. Figure 3, as well as other figures, can be reinterpreted by considering the relation displayed in Figure 4 between altitude and elapsed time of the considered trajectory. Note that the term "altitude" here always refers to the distance of the receiver from Earth's surface. As illustrated in Figures 5 and 6 (and equivalently in figures 6 and 7 of [7]), the analysis of the dynamics has shown that the carrier frequency can be affected by Doppler shifts and Doppler rates of up to 20 kHz and up to 3 Hz/s, respectively, at the Moon altitude (when the signals are weaker) and of up to 60 kHz and up to 65 Hz/s at the very beginning of the MTO (when the signals are stronger). Note that the spikes at the beginning of the orbit (of up to 60 kHz and up to 65 Hz/s) are due to the very high velocity of the receiver at the perigee of the MTO. This poses additional challenges for the acquisition and tracking of the satellite signals. Finally, considering only the four strongest received signals, the Geometric Dilution of Precision (GDOP) is typically higher than 1000 at the Moon altitude as shown later in The WeakHEO Receiver section (see Figure 9), while due to the very weak signals the receiver noise and accordingly the ranging error can be much larger than on Earth. For example, the code tracking error due to thermal noise of an L1 C/A code signal at −159 dBm can reach peaks above 6 m [6].

THE WEAKHEO RECEIVER

Following the identification of the signal performances for an MTO and the consequent requirements, the GNSS team of the ESPLAB of the École Polytechnique Fédérale de Lausanne (EPFL) in Switzerland has developed an FPGA-based proof of concept demonstrator for lunar missions. This platform is called the "*WeakHEO*" receiver.

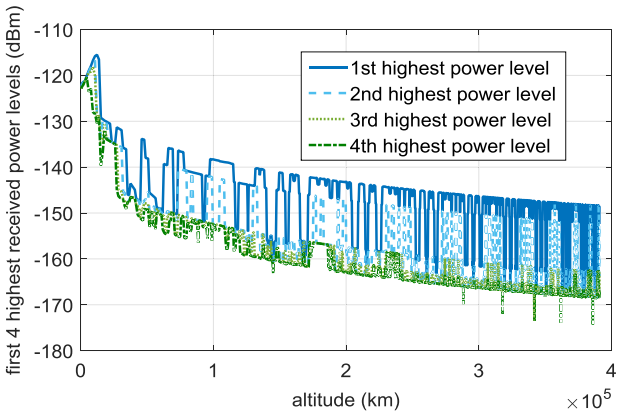

Fig. 3–First, second, third, and fourth highest received power levels of the GPS L1 C/A signals as a function of time, during the full considered trajectory, by assuming a 0-dBi receiver antenna gain. [Color figure can be viewed at wileyonlinelibrary.com and www.ion.org]

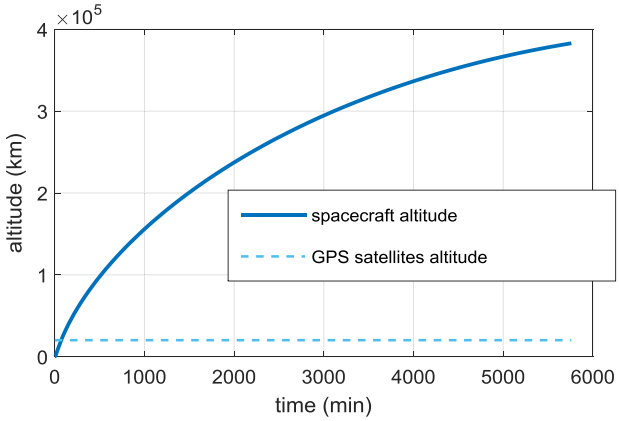

Fig. 4–Relation between altitude and time during the considered MTO and GPS constellation altitude. [Color figure can be viewed at wileyonlinelibrary.com and www.ion.org]

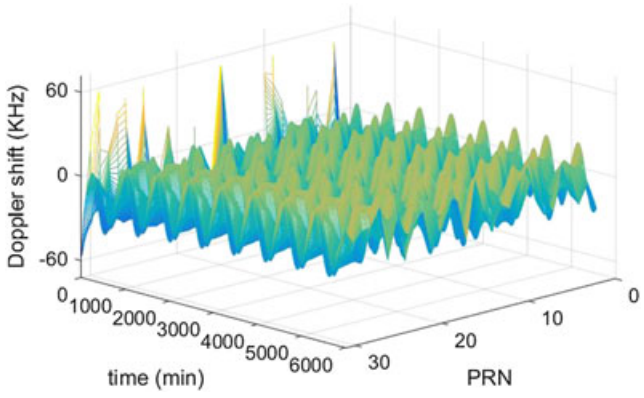

Fig. 5–Doppler shift of received GPS L1 C/A signals across the MTO. [Color figure can be viewed at wileyonlinelibrary.com and www.ion.org]

The architecture of the *WeakHEO* receiver is shown in Figure 7. The receiver consists of a low noise amplifier (LNA), a Tri-band (L1, L2, L5) RF front end, an Altera Stratix III FPGA with DDR2 memory, and an associated PC. The RF front end down-converts GNSS signals on the L1, L2, and L5 carrier frequencies to a common IF frequency of 53.78 MHz and samples the signal at 40.96 MHz with 4-bit resolution. The digital samples are passed in parallel to the FPGA or can be streamed and recorded directly via a USB interface to a PC for offline processing. The FPGA contains a softcore NIOS II processor and performs all the high sensitivity acquisition, tracking, and navigational data decoding processes. Raw measurements (pseudoranges, pseudorange rates, signal parameters, time, etc.) are passed to the PC through a UART interface at a rate of 0.1 Hz. The PC then performs the navigation solution in real time or can record and compute the orbital filter calculations offline.

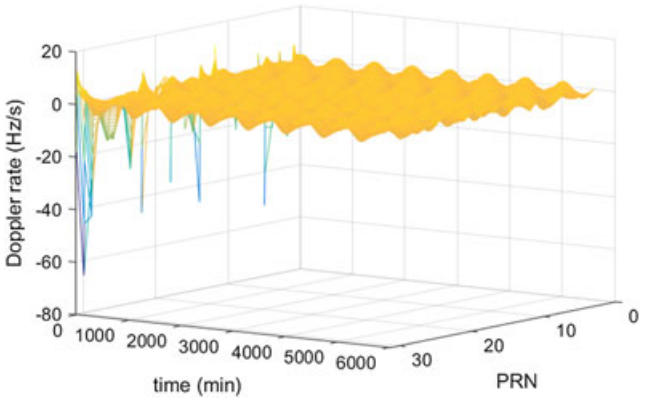

Fig. 6–Rate of change of Doppler shift of received GPS L1 C/A signals across the MTO. [Color figure can be viewed at wileyonlinelibrary.com and www.ion.org]

The receiver is currently limited to six channels because of the processing load required to achieve the high sensitivity acquisition, data demodulation, and tracking. However, the current hardware has demonstrated acquisition and tracking of signals with signal levels down to −159 dBm (equivalent C/N_0 = 15 dB-Hz) in low dynamics without assistance and further improvement demonstrated in high dynamics using the orbital filter aiding, as described in the Orbital Filter Aiding to the GNSS Module section. A second version of the receiver, "*WeakHEO 2*," is planned which will vastly improve the processor capability and provide much more efficient processing of the algorithms. The raw measurement output rate will also be increased to at least 1 Hz.

As in our previous work and in others, we assumed 10 dBi gain antenna at the receiver position. Such a gain value could be achieved during the whole trajectory by electronically steering an array of antennas on board the space vehicle, or if the size of the vehicle is big enough, by equipping it with more than one receiver antenna placed on different

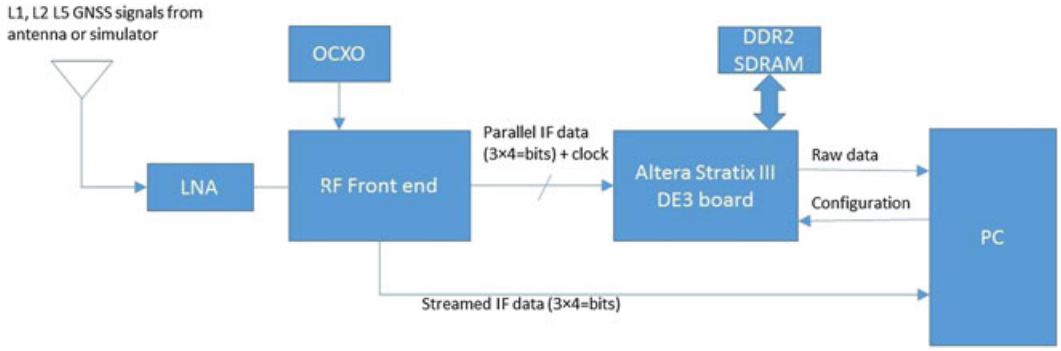

Fig. 7–WeakHEO receiver architecture. [Color figure can be viewed at wileyonlinelibrary.com and www.ion.org]

faces, as in other research efforts, e.g., in [11], in order that at least one antenna points in the GNSS satellites direction (at very high altitudes, this corresponds to an Earth-pointing space vehicle approximately).

As explained the Mission Scenario Description section, during the whole considered trajectory, the fourth highest GPS L1 C/A received signal at receiver antenna does not go below −168.5 dBm (see Figure 3). This means that, by assuming a 10-dBi receiver antenna gain, a receiver sensitivity of −159 dBm will allow for the simultaneous detection (with a certain probability) of at least 4 GNSS satellites and the computation of a navigation solution for the entire selected MTO trajectory.

Figures 8 and 9 show respectively the number of available satellites and the consequent GDOP during the full considered MTO for the *WeakHEO* receiver, which has 6 channels and a sensitivity of −159 dBm. Note that in our simulations the few signals that cross the ionosphere have been discarded when the receiver is above it, in order to prevent any atmospheric delay, which could be a significant source of error in the ranging measurements. A much more detailed description of the *WeakHEO* receiver can be found in [7].

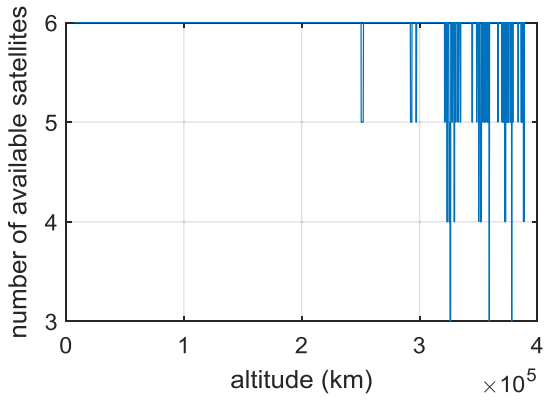

Fig. 8–Number of available GPS satellites for each altitude value of the considered MTO. [Color figure can be viewed at wileyonlinelibrary.com and www.ion.org]

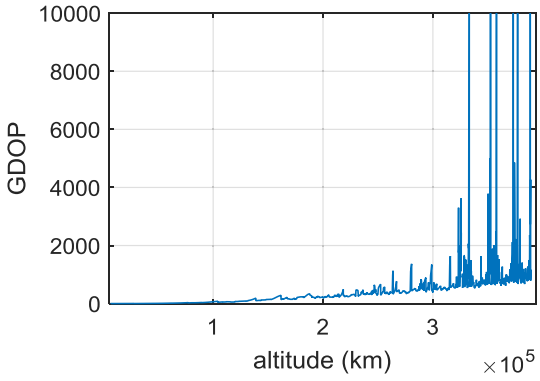

Fig. 9–GDOP for each altitude value of the full considered MTO. The GDOP has been computed considering the six or less available GPS signals with the best GDOP. The sensitivity of −159 dBm of the WeakHEO receiver has been assumed. [Color figure can be viewed at wileyonlinelibrary.com and www.ion.org]

THE ORBITAL FILTER

An adaptive extended Kalman filter (EKF) has been adopted here, which integrates the single-epoch least-squares position and velocity solutions that are computed using the pseudoranges and the pseudorange rates output by the *WeakHEO* GPS receiver, together with the position and velocity predicted by an orbital forces model. One advantage of using the single-epoch least-squares solution as observation is that there is no linearization error in the orbital filter computation of the observation partial derivatives with respect to the states since the state vector is identical to the measurements vector. Filtering the position and velocity solution keeps the GNSS receiver as independent (fault tolerant system); thus, it is simpler, more robust, and has a clearer approach. However, in our previous study [13], we have also shown that, although more complex, filtering the raw pseudoranges and pseudorange rates can in general be more efficient, especially when less than four satellites are available (since the update of the estimations in the filter can still be achieved), leading to a higher navigation accuracy as also

reported in [2]. A second version of the EKF filter using pseudoranges and pseudorange rates (as described in [3, 4]) will thus be implemented in the *WeakHEO 2* GPS receiver, currently under development, that will provide a ten times higher raw data output rate than the current platform.

In this work then, the measurement vector z can be written as

$$\boldsymbol{z} = \begin{bmatrix} \boldsymbol{x}_{GPS} \\ \boldsymbol{v}_{GPS} \end{bmatrix} \tag{1}$$

where $\boldsymbol{x}_{GPS} = [x_{GPS}\ y_{GPS}\ z_{GPS}]^T$ and $\boldsymbol{v}_{GPS} = [u_{GPS}\ \ v_{GPS}\ \ w_{GPS}]^T$ are respectively the position and velocity vectors computed through a least-squares estimator.

While the state vector $\boldsymbol{x}$ contains the position and velocity components of the receiver, i.e.,

$$\boldsymbol{x} = [\,x\ \ y\ \ z\ \ u\ \ v\ \ w\,]^T \tag{2}$$

Note that an estimation of clock bias and clock drift is provided as part of the least-squares solution, together with the position and velocity used as input of the filter. However, in addition, these clock bias and drift estimates can be refined using the more accurate filtered position and velocity solution (and the position and velocity of the GNSS satellites, already available from the ephemeris). In a Kalman filter-based dynamic orbit determination, measurements are fused with their prediction computed by propagating the kinematic state through a mathematical model of the dynamics (the process model of the filter). The dynamics of a spacecraft during an MTO is a function of several orbital forces. Depending on the altitude, each orbital force can have a weaker or stronger effect on the spacecraft kinematics. Thus, as shown in Table 2, the designed orbital filter is characterized by three different configurations of the process model based on the altitude of the receiver, in order to lower the computational burden. For example, it would not be worth modeling the gravitational perturbations due to the Sun when the spacecraft is in low Earth orbit (LEO), as well as Earth's oblateness when the receiver is close to Moon. The computation of Earth's gravitational potential and the acceleration of the spacecraft due to the gravitational effect of the Sun and the Moon have been modeled according to [12], while the effect of the SRP is modeled according to [13], as described in [14].

Table 3 reports the EKF algorithm, where $\boldsymbol{x}(t)$ is the true state vector at time t, $\boldsymbol{w}_s(t)$ is the continuous system noise vector, $\boldsymbol{G}(t)$ is the continuous system noise distribution matrix, $\hat{\boldsymbol{x}}_{\bar{k}}$ is the *a priori* state estimate at a time step ?, $\hat{\boldsymbol{x}}_{k-1}^{+}$ is the *a posteriori* state estimate at a time step k–1, $\boldsymbol{\Phi}_{k-1}$ is the state transition matrix at a time step k–1, $\boldsymbol{P}_k^-$ is the *a priori* estimate error covariance at a time step k, $\boldsymbol{P}_{k-1}^{+}$ is *a posteriori* estimate error covariance at a time step k–1, $\boldsymbol{Q}_{k-1}$ is the discrete process noise covariance a time step k–1, $\boldsymbol{R}_k$ is the discrete measurement noise covariance at a time step k, $\boldsymbol{H}_k$ is the observations matrix at a time step k, $\boldsymbol{K}_k$ is the Kalman gain at a time step k, z_k is the measurement vector at a time step k, $\boldsymbol{h}(\hat{\boldsymbol{x}}_{\bar{k}})$ is the observation function of the state used to predict the measurement, $\delta \mathbf{z}_k^-$ is the innovation measurement vector at a time step k, and $\boldsymbol{I}$ is a unit matrix.

According to [15] the state transition matrix can be approximated as

$$\boldsymbol{\Phi}_{k-1} \approx e^{\boldsymbol{F}_{k-1}(\tau_s)} \cong (I + \boldsymbol{F}_{k-1}\tau_s), \tag{3}$$

where τ_s is the propagation interval and

$$\boldsymbol{F}_{k-1} = \left.\frac{\partial \boldsymbol{f}(\boldsymbol{x}, t_k)}{\partial \boldsymbol{x}}\right|_{\boldsymbol{x}=\hat{\boldsymbol{x}}_{k-1}^{+}} \tag{4}$$

is the linearized system matrix about the *a posteriori* state vector estimate at time t_{k-1}. Here

Table 2—Configurations of the Process Model as Function of the Distance from Earth's Center, r

Configurations	Modeled perturbations
$\boldsymbol{r} < 9600\ km$	• Spherical harmonics of Earth gravitational potential up to 6th degree and 6th order
$9600\ \boldsymbol{km} \le \boldsymbol{r} \le 50\ 000\ \boldsymbol{km}$	• Spherical harmonics up to 2nd degree and 2nd order • solar radiation pressure (SRP)
$\boldsymbol{r} > 50\ 000\ km$	• Gravitational perturbations due to the Sun and the Moon • 1st order Earth gravity • SRP • Gravitational perturbations due to the Sun and the Moon

Table 3—EKF Algorithm [15]

Quantity	Formulation
System dynamic model	$\dot{\boldsymbol{x}}(t) = \boldsymbol{f}(\boldsymbol{x}(t), t) + \boldsymbol{G}(t)\boldsymbol{w}_s(t)$
Predicted state vector	$\hat{\boldsymbol{x}}_k^- = \hat{\boldsymbol{x}}_{k-1}^{+} + \int_{k-1}^{k} \boldsymbol{f}(\hat{\boldsymbol{x}}, t)\, dt$
Predicted system noise covariance matrix	$\boldsymbol{P}_k^- = \boldsymbol{\Phi}_{k-1}\boldsymbol{P}_{k-1}^{+}\boldsymbol{\Phi}_{k-1}^T + \boldsymbol{Q}_{k-1}$
Kalman Gain matrix	$\boldsymbol{K}_k = \boldsymbol{P}_k^- \boldsymbol{H}_k^T \left(\boldsymbol{H}_k \boldsymbol{P}_k^- \boldsymbol{H}_k^T + \boldsymbol{R}_k\right)^{-1}$
Corrected state estimate	$\hat{\boldsymbol{x}}_k^{+} = \hat{\boldsymbol{x}}_k^- + \boldsymbol{K}_k\left(z_k - \boldsymbol{h}(\hat{\boldsymbol{x}}_k^-)\right) = \hat{\boldsymbol{x}}_k^- + \boldsymbol{K}_k \delta \boldsymbol{z}_k^-$
Corrected system noise covariance matrix (Joseph form)	$\boldsymbol{P}_k^{+} = (\boldsymbol{I} - \boldsymbol{K}_k\boldsymbol{H}_k)\boldsymbol{P}_k^-(\boldsymbol{I} - \boldsymbol{K}_k\boldsymbol{H}_k)^T + \boldsymbol{K}_k\boldsymbol{R}_k\boldsymbol{K}_k^T$

the matrix $\boldsymbol{F}_{k-1}$ is computed adopting the complex-step derivative approximation, described in [16, 17]. In this case where the single point least-squares navigation solution is used as observation,

$$\boldsymbol{h}\left(\hat{\boldsymbol{x}}_k^-, t_k\right) = \hat{\boldsymbol{x}}_k^- \tag{5}$$

and

$$\boldsymbol{H}_k = \left.\frac{\partial \boldsymbol{h}\left(\hat{\boldsymbol{x}}_{\bar{k}}, t_k\right)}{\partial \boldsymbol{x}}\right|_{\boldsymbol{x}=\hat{\boldsymbol{x}}_{\bar{k}}} = \boldsymbol{I} \tag{6}$$

The discrete process noise covariance has been defined constant over time, as

$$\boldsymbol{Q} = \operatorname{diag}\left(\sigma_x^2, \sigma_y^2, \sigma_z^2, \sigma_u^2, \sigma_v^2, \sigma_w^2\right) \tag{7}$$

where $\sigma_x^2, \sigma_y^2, \sigma_z^2$ and $\sigma_u^2, \sigma_v^2, \sigma_w^2$ are respectively the variance of the position components and of the velocity components, set by adjusting their values by trial until satisfactory performance was achieved (the values are reported in [4]). The discrete measurement noise covariance has been defined as a function of the measurement quality as follows:

$$\boldsymbol{R}_k = diag\left(\sigma_{\rho_k}^2, \sigma_{\rho_k}^2, \sigma_{\rho_k}^2, \sigma_{\dot{\rho}_k}^2, \sigma_{\dot{\rho}_k}^2, \sigma_{\dot{\rho}_k}^2\right) \cdot GDOP_k \tag{8}$$

Where $\sigma_{\rho_k}^2$ and $\sigma_{\dot{\rho}_k}^2$ are respectively the average variance value at time step k; of the estimated pseudoranges errors $\sigma_{\rho_{k_i}}^2$ and the average variance value of the estimated pseudorange rate errors $\sigma_{\dot{\rho}_{k_i}}^2$, while $GDOP_k$ is the estimated GDOP value at time step k. The variance $\sigma_{\rho_{k_i}}^2$ for the i-th GPS satellite is estimated, assuming a constant variance for GPS broadcast clock, broadcast ephemeris, atmospheric delay, multipath, and receiver noise, and considering the thermal noise code tracking jitter σ_{tDLL} function of the carrier-to-noise ratio C/N_0 [4]. The variance $\sigma_{\dot{\rho}_{k_i}}^2$ is computed from the Doppler tracking jitter σ_f, as a function of the carrier-to-noise ratio C/N_0 [4]. At the Moon altitude where the signals are very weak, their variance can be much higher, as described in [6]. A much more detailed description about the model used to estimate $\sigma_{\rho_{k_i}}^2$ and $\sigma_{\dot{\rho}_{k_i}}^2$ can be found in our previous study [4].

NAVIGATION PERFORMANCE

Simulation Models

The GPS L1 C/A signals at the receiver position for the considered full MTO and for the considered portion of it were generated by our Spirent 8000 simulator. In order to correctly reproduce realistic signal power levels at the receiver position, taking into account the transmitting antenna and the signal propagation losses during the MTO, the simulator has been set by considering:

- a GPS constellation made of 31 GPS satellites, allocated in the six orbital planes, according to the GPS ICD [18];
- 3D GPS antenna patterns, as described in our previous study [4, 6].
- a power reference level (guaranteed minimum signal level) of −128.5 dBm according to [18]. A value of +3 dB has been used to match the performance obtained when using the simulator with the performance obtained when real signals are received. The transmitted signal powers are typically from 1 to 5 dB higher than the minimum received signal power [19]; thus, an intermediate value of 3 dB has been chosen; and
- a receiver antenna gain of 10 dBi as already stated in The WeakHEO Receiver section.

According to [20], it is possible to calculate the carrier-to-noise density ratio C/N_0 (in dB-Hz) from the received power P_r (in dBm) by using the following formula, valid for a front-end noise figure of 2 dB and an effective antenna temperature of 130 K:

$$C/N_0 = P_r + 174 \tag{9}$$

A received signal level of −159 dBm then corresponds to a C/N_0 of 15 dB-Hz.

When using a GNSS simulator, the effective antenna temperature is the room temperature, which increases the noise. In that case the carrier-to-noise ratio can be obtained as

$$C/N_0 = P_r + 172 \tag{10}$$

A received signal level of −157 dBm then corresponds to a C/N_0 of 15 dB-Hz for testing with the GNSS simulator.

Simulation Results

The navigation performance of the orbital filter over the full MTO has been simulated by modeling in MATLAB the raw measurements of the *WeakHEO* receiver, according to all its specifications and characteristics described in The WeakHEO Receiver section. Pseudoranges, pseudorange rates, and GPS satellite kinematics estimates were modeled as described in detail in our previous study [14] as a function of the true kinematics of the receiver and of the GPS satellite positions and received powers as provided by the PosApp software of Spirent. In addition, in order to optimize the six signals selection (only six channels were available because of the resource limitations), a selection algorithm has been implemented, which selects the

combination of the six visible (accounting for the *WeakHEO* acquisition and tracking sensitivity of −159 dBm) with the best GDOP. Figures 10 and 11 show respectively the 3D position error and the 3D velocity error of the orbital filter estimation for each altitude value of the full considered MTO. The filtered state vector at the starting point of the MTO (in LEO) was initialized with the single-epoch least-squares solution. As expected, both position and velocity errors increase with the altitude because of the combined effect of GDOP (see Figure 9) and range error increasing. The GDOP increase is due to the worsening with altitude of the relative geometry between the receiver and the GPS satellites. Indeed, with the increase in altitude of the receiver above the constellation, the GPS satellites are more and more concentrated in a smaller angle of sphere. The range error increasing is instead an effect of the decreasing C/N_0 with the distance from the GPS transmitters, as described in detail in [6].

HIL Tests Results

The *WeakHEO* proof of concept receiver has been tested in simulated scenarios at a number of different locations in the MTO. Here we focus on testing a representative 1 h portion of the MTO which starts approximately at the average distance of the Moon from the center of Earth of 384,400 km. The filtered state vector at the starting point of the considered MTO portion was initialized with the filtered state vector expected for that point of the MTO, provided by the simulation results of Figures 10 and 11.

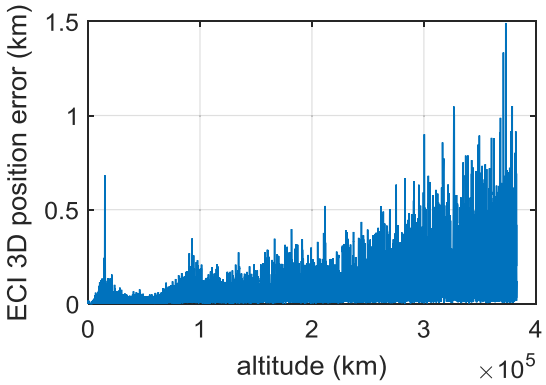

Fig. 10–Orbital filter 3D position error for the full considered MTO. [Color figure can be viewed at wileyonlinelibrary.com and www.ion.org]

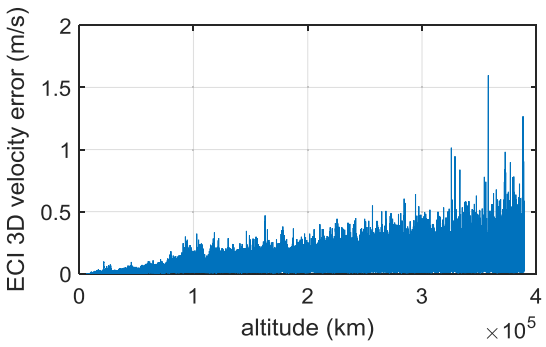

Fig. 11–Orbital filter 3D velocity error for the full considered MTO. [Color figure can be viewed at wileyonlinelibrary.com and www.ion.org]

Figures 12 and 13 illustrate, respectively, the 3D position error and the 3D velocity error of the single-epoch least-squares solution, of the propagated solution by the orbital forces model, and of the EKF-filtered solution for the considered portion at the Moon altitude. The filtered solution that converges to an error of about 230 m is much more accurate than both the very noisy single-epoch least-squares solution (that reaches peaks of almost 14 km error) and the propagated solution that shows a drift of approximately 1 km/h. Figures 14 and 15 show, respectively, the position and velocity error in the radial, in-track, and cross-track directions. As expected, the main least-squares error is in the radial direction. Figure 16 illustrates the GDOP for the considered portion, which also explains the large positioning error for the single-epoch least-squares solution. Figures 17 and 18 show, respectively, the accuracy in the Doppler and Doppler rate estimation when using the filtered solution. The error of such estimation corresponds to the aiding error as described in the Orbital Filter Aiding to the GNSS Module section.

ORBITAL FILTER AIDING TO THE GNSS MODULE

In this section, will we show the performance of ESPLAB's FPGA-based *WeakHEO* receiver during acquisition and tracking tests at the Moon altitude. This is intended to validate that the sensitivity of 15 dB-Hz can be achieved. The effects of Doppler and Doppler rate aiding are shown.

In [21], the required accuracy of Doppler aiding is shown for signal levels in the range of 5 to 10 dB-Hz. However, perfect synchronization and wipe-off of the navigational data sequence is assumed allowing the acquisition to use coherent integrations beyond the data bit boundary. The *WeakHEO* receiver is assumed to be a stand-alone receiver with the orbital filter integrated and a low-rate communication interface to the spacecraft platform. Therefore, only aiding from the orbital filter is considered so the receiver can work autonomously. Knowledge of the full navigational data sequence is not assumed, and data wipe-off is not used in any of the following tests.

In acquisition, the receiver uses coherent accumulations which are the length of a full navigation data bit (20 ms for GPS C/A code). The

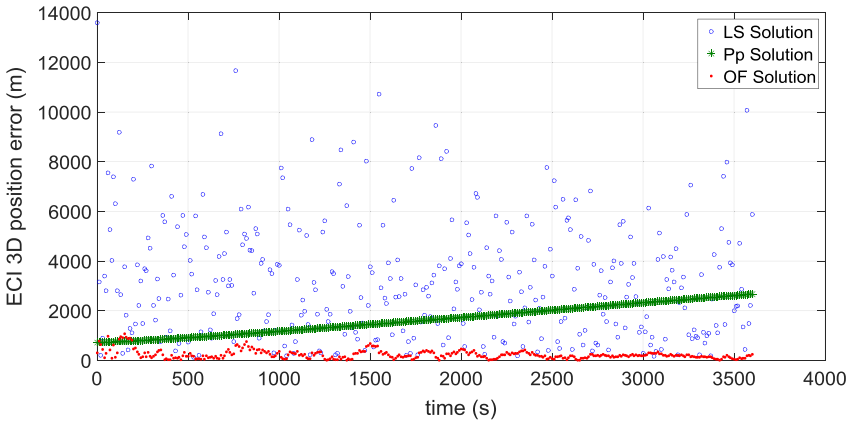

Fig. 12–3D position error for the considered portion at the Moon altitude of the single-epoch least-squares solution (in blue); the EKF-filtered solution (in red); and the propagated solution (in green). [Color figure can be viewed at wileyonlinelibrary.com and www.ion.org]

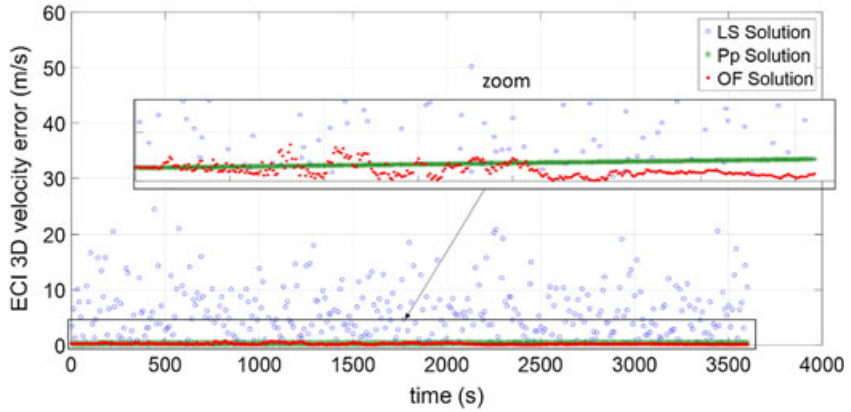

Fig. 13–3D velocity error for the considered portion at the Moon altitude of the single-epoch least-squares solution (in blue); the EKF-filtered solution (in red); and the propagated solution (in green). [Color figure can be viewed at wileyonlinelibrary.com and www.ion.org]

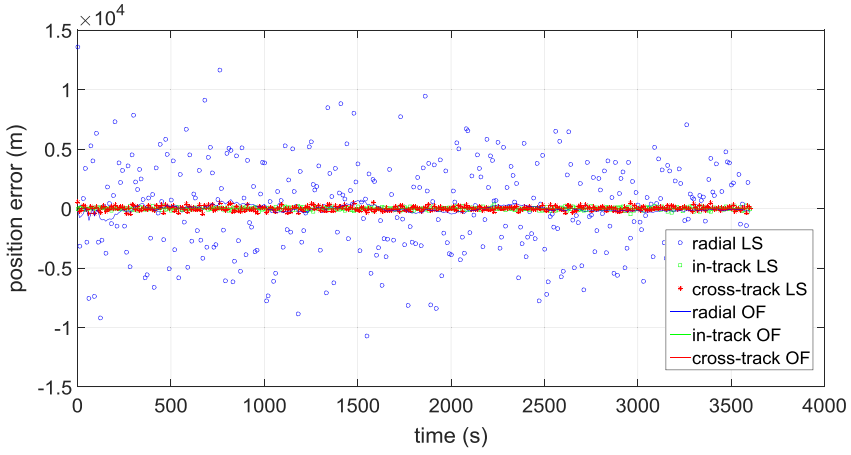

Fig. 14–Radial, along track, and cross-track position error of the single-epoch least-squares (LS) solution and of the filtered solution (OF) for the considered portion at the Moon altitude. [Color figure can be viewed at wileyonlinelibrary.com and www.ion.org]

results are then non-coherently accumulated to gain further sensitivity. To reduce the effect of the data bit transitions, a number of different accumulations are formed with different starting points. Ideally, for GPS C/A code, we would have 20 accumulations spaced 1 ms apart. However, to limit the impact on

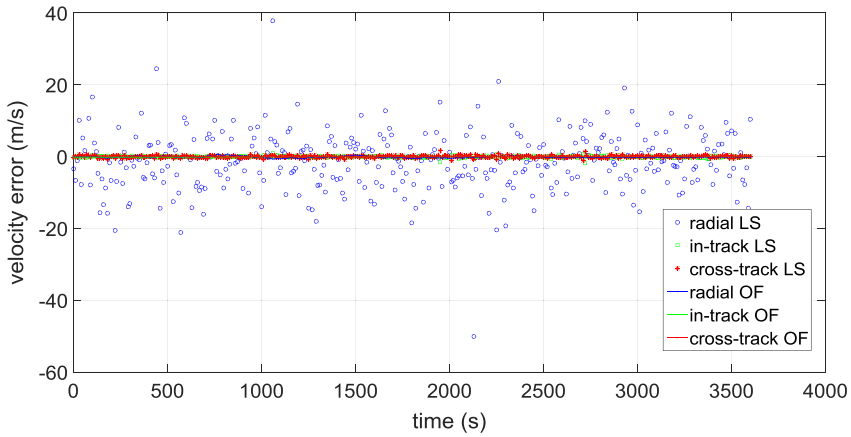

Fig. 15–Radial, along track, and cross track velocity error of the single-epoch least-squares solution (LS) and of the filtered solution (OF) for the considered portion at Moon altitude. [Color figure can be viewed at wileyonlinelibrary.com and www.ion.org]

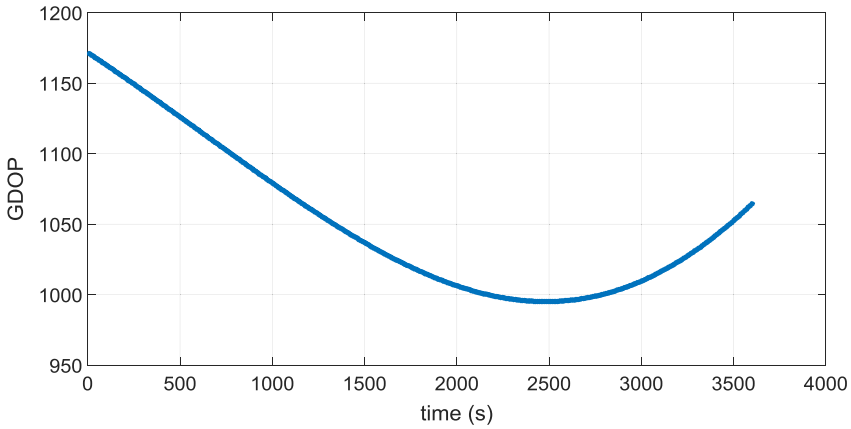

Fig. 16–GDOP. [Color figure can be viewed at wileyonlinelibrary.com and www.ion.org]

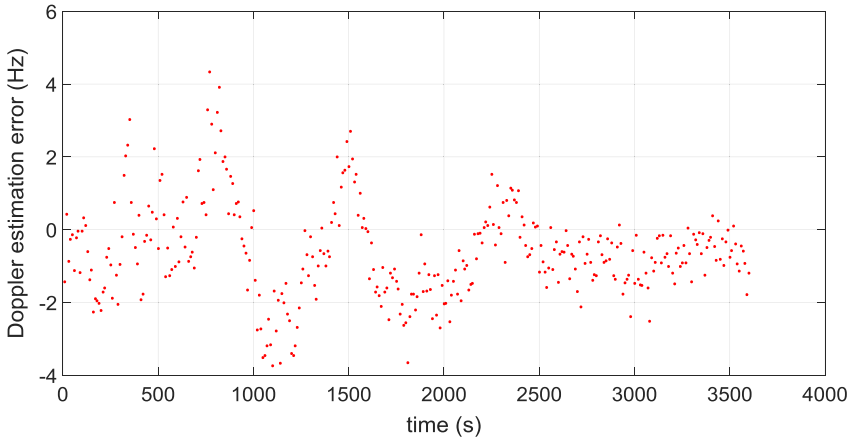

Fig. 17–Error of the Doppler estimated by the orbital filter. [Color figure can be viewed at wileyonlinelibrary.com and www.ion.org]

the FPGA resources we form ten accumulations spaced 2 ms apart. This results in a worse-case 0.915-dB signal power loss where the accumulation is misaligned by 1 ms with respect to the data transition. In the acquisition tests that follow, 475 non-coherent acquisitions have been used which results in a 9.5 s total accumulation time. The acquisition parameters used to achieve a sensitivity of 15 dB-Hz are given in Table 4. We define the maximum tolerable Doppler rate error

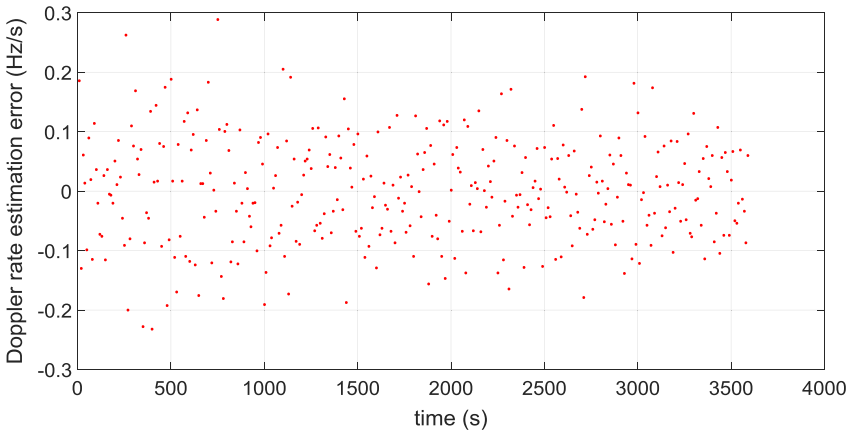

Fig. 18–Error of the Doppler rate estimated by the orbital filter. [Color figure can be viewed at wileyonlinelibrary.com and www.ion.org]

as corresponding to the Doppler rate which implies a shift of one frequency bin during the accumulation time. Using typical derivations from [19] and [21], the detection threshold is chosen such that the single trial probability of detection is theoretically 0.95 at 15 dB-Hz and probability of false alarm is 10^{-3}.

Final bit synchronization and navigational data decoding is performed after the acquisition stage. In the tracking channel, 20 branches, spaced 1 ms apart, are then formed and accumulated to confirm the bit edge position. During this process, the tracking channel operates a low bandwidth FLL (0.2 Hz) initialized with the estimation of Doppler, Doppler rate, code offset, and bit position from the acquisition engine. Details of the acquisition times can be found in [7].

The acquisition and tracking capability of the *WeakHEO* receiver has been tested at multiple points across an MTO. Here, we concentrate on the acquisition and tracking of signals while at the Moon altitude in the scenario of the Mission Scenario Description section.

Table 4—Acquisition Parameters

Quantity	Value
C/*N0* (dB-Hz)	15
Sampling rate (MHz)	4.096
Quantization (bit)	4
Quantization loss (dB)	0.05
Coherent integration time (ms)	20
Coherent gain (dB)	46
Frequency search step (Hz)	25
Worst case frequency mismatch loss (dB)	0.91
Code search step (chip)	0.25
Worst case code alignment loss (dB)	1.16
Data bit alignment loss (dB)	0.92
Squaring loss (dB)	5.73
Final desired SNR (dB)	16
Non-coherent gain required (dB)	26.77
Number of non-coherent integration	475
Total accumulation time (s)	9.5
Maximum tolerable Doppler rate error (Hz/s)	2.63

The success rate of the acquisition engine with Doppler and Doppler rate aiding from the orbital filter across signals with different carrier-to-noise density ratios (C/No) is shown in Figure 19. Here 25 trials were performed at each signal level and the success rate recorded for the acquisition, bit synchronization, and data decoding stages. The simulator output power is also displayed in Figure 19. The navigation data are decoded by averaging across 40 repeated frames of data. The parity of each word is checked, and the time of the week used to determine if decoding was successful.

The results of Figure 19 are slightly worse but within 1 dB of the expected performance from theoretical analysis. Clearly, the receiver is limited by its ability to synchronize and decode the navigation data before the acquisition limit is encountered. Despite this, at 15 dB-Hz, the receiver is still able to acquire and decode the navigational data with a success rate of around 60 percent for each attempt.

To demonstrate the potential benefit of Doppler aiding to the receiver's tracking loops we use a conventional frequency locked loop (FLL). With no knowledge of the data bits, the normalized arctangent cross-product over dot product Costas type discriminator is used. When operating with very weak signal conditions, we found the denominator (the dot product) needs to be limited or filtered to avoid singularities. For our FLL implementation, we use a cumulative moving average filter of the dot product over n correlations as follows:

$$DP_k == DP_{k-1} + \frac{1}{n+1}\left(I_{P,k-1}I_{P,k} + Q_{P,k-1}Q_{P,k} - DP_{k-1}\right) \tag{11}$$

where I_P and Q_P are the in-phase and quadrature accumulations from the receiver's correlator. In the

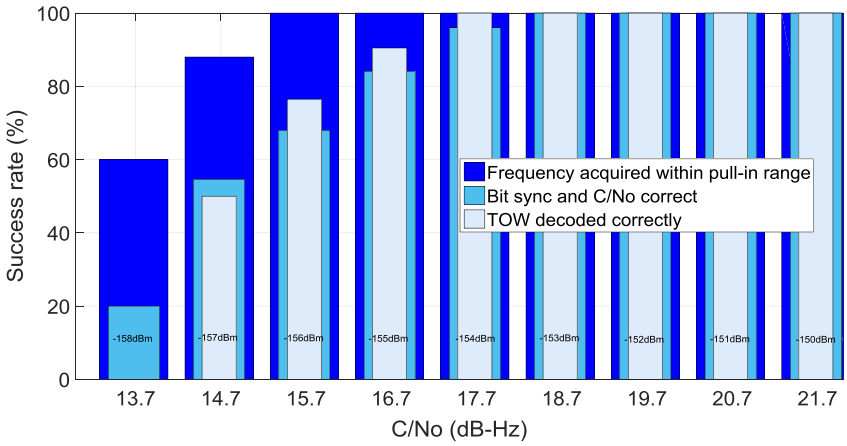

Fig. 19–Sucess rate of GPS L1 C/A acquisition stages with varying signal levels. [Color figure can be viewed at wileyonlinelibrary.com and www.ion.org]

tests that follow we use $n = 150$ with an accumulation time $\tau_a = 20\ ms$. The normalized discriminator is then formed as

$$\delta\tilde{f}_{ca,k} == \frac{1}{2\pi\tau_a}\arctan\left(\frac{\left(I_{P,k-1}Q_{P,k} - I_{P,k}Q_{P,k-1}\right)\times\hat{d}}{DP_k}\right) \tag{12}$$

where $\hat{d}$ is estimated sign of the data bit, estimated from the dot product of the current and previous correlations:

$$\hat{d} = \text{sign}\left(I_{P,k-1}I_{P,k} + Q_{P,k-1}Q_{P,k}\right) \tag{13}$$

A second order FLL filter is then implemented following [15] where the estimates of Doppler frequency $\Delta\tilde{f}_{ca}$ and Doppler rate $\Delta\dot{\tilde{f}}_{ca}$ are updated as follows:

$$\begin{aligned}\Delta\tilde{f}^{+}_{ca,k} &= \Delta\tilde{f}^{-}_{ca,k} + K_{cf1}\delta\tilde{f}_{ca,k}\\ \Delta\dot{\tilde{f}}^{+}_{ca,k} &= \Delta\dot{\tilde{f}}^{-}_{ca,k} + \frac{K_{cf2}}{\tau_a}\delta\tilde{f}_{ca,k}\end{aligned} \tag{14}$$

The loop gains are set to achieve the desired loop response and carrier loop bandwidth B_{L_CF} as follows [22]:

$$\begin{aligned}K_{cf1} &= 3.4B_{L\_CF}\tau_a\\ K_{cf2} &= 2.04(B_{L\_CF}\tau_a)^2\end{aligned} \tag{15}$$

Currently, we only have an offline version of the orbital filter running. Future work will allow real-time operation within the *WeakHEO* processor. However, we can assess the benefit to tracking using stored IF data from the *WeakHEO* receiver's RF front end during the Moon altitude scenario.

The rate at which Doppler aiding can be provided to the tracking loops depends on how often the orbital filter can be iterated by the on-board processor. Here we have tested 1 s and 10 s update rates of the orbital filter.

When Doppler aiding is available, a technique named "vector hold tracking" is used from [23]. This technique is well suited to this operational scenario where a few stronger GNSS signals can aid the weaker ones along with the orbital filter. The FLL is used to track strong signals. When the signal level is estimated to be under a certain C/No threshold (15 dB-Hz in our case), the estimated Doppler from the tracking loop is compared with that of the orbital filter. If the difference is greater than a threshold (in our case 3.125 Hz, one quarter of the FLL pull-in range), the Doppler estimate is updated with the Doppler from the orbital filter. The FLL is then used to update the Doppler estimate between available aiding updates. The Doppler rate estimate from the orbital filter is currently only used for acquisition and not during tracking.

Following the update, the estimates are predicted forward to the next iteration by

$$\begin{aligned}\Delta\tilde{f}^{-}_{ca,k+1} &= \Delta\tilde{f}^{+}_{ca,k} + \Delta\dot{\tilde{f}}^{+}_{ca,k}\tau_a\\ \Delta\dot{\tilde{f}}^{-}_{ca,k+1} &= \Delta\dot{\tilde{f}}^{+}_{ca,k}\end{aligned} \tag{16}$$

The carrier N/CO is then updated as

$$\hat{f}_{ca,NCO,k+1} = f_{IF} + \Delta\tilde{f}^{-}_{ca,k+1} \tag{17}$$

where F_{IF} is the intermediate frequency chosen in the receiver's RF front end.

The code tracking loop of the receiver is a first-order loop aided by the carrier loop and uses a bandwidth of 0.1 Hz. Figure 20 shows the expected FLL jitter and a conservative loss of lock threshold for the FLL assuming thermal noise is the only error

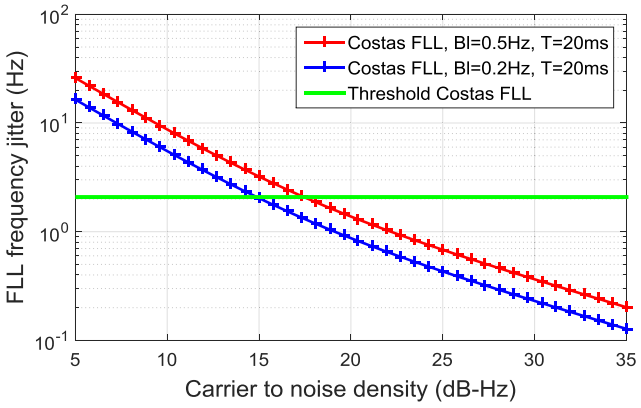

Fig. 20–FLL jitter versus C/No. [Color figure can be viewed at wileyonlinelibrary.com and www.ion.org]

source. This indicates that in the presence of navigation data flips, we may need to use bandwidth as low as 0.2 Hz to operate at 15 dB-Hz.

To test the tracking threshold during the Moon altitude scenario, the signal level was progressively reduced during the scenario to below 12 dB-Hz. Figures 21 and 22 show examples of the frequency tracking error of PRN 26 during the scenario with FLL bandwidth of 0.5 Hz and 0.2 Hz, repectively.

The FLL with 0.5 Hz bandwidth loses lock at around 15 dB-Hz and the 0.2 Hz bandwidth around 13 dB-Hz. Also shown is the same dataset reprocessed with aiding from the orbital filter at 1 s and 10 s update rates. In both cases, the 1 s update rate from the orbital filter shows a significant improvement on the stand-alone tracking. If aiding from the orbital filter is only available every 10 s, an oscillation can occur as the FLL Doppler estimate generated between aiding updates diverges from the correct frequency. Prolonged behavior like this would result in complete loss of code correlation as well as the carrier.

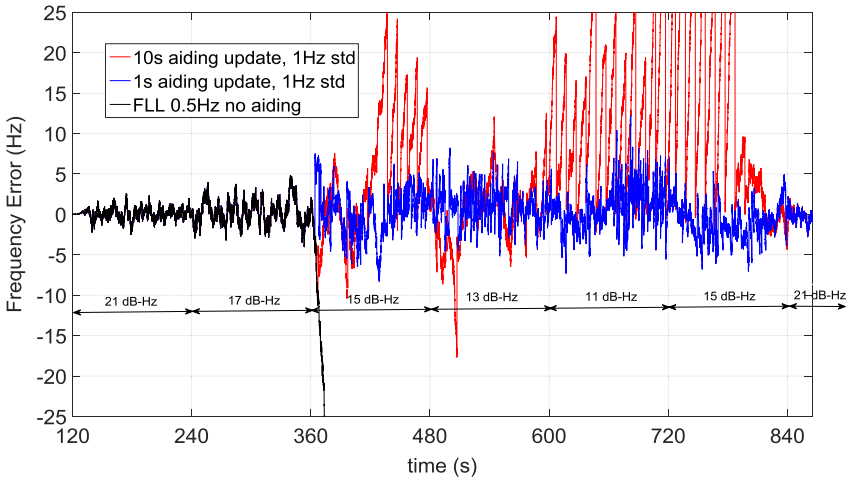

Fig. 21–Frequency errors of tracking PRN 26 with 0.5 Hz bandwidth FLL and orbital filter aiding. [Color figure can be viewed at wileyonlinelibrary.com and www.ion.org]

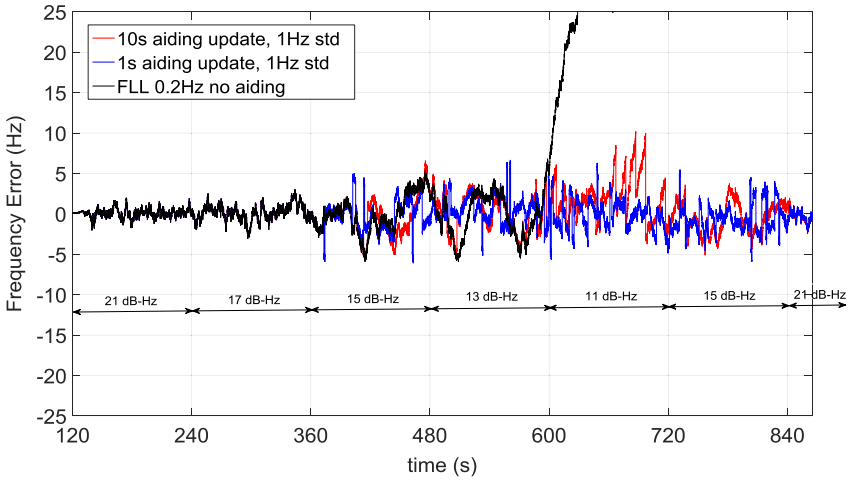

Fig. 22–Frequency errors of tracking PRN 26 with 0.2 Hz bandwidth FLL and orbital filter aiding. [Color figure can be viewed at wileyonlinelibrary.com and www.ion.org]

First, we artificially introduce random errors to find the accuracy required by the tracking. With a Doppler aiding accuracy of 1 Hz (1σ) and a one s update rate, tracking is sustained down to 11 dB-Hz, and the error maintained well within the FLL pull-in range (±12.5 Hz). This performance is repeated across the other satellites in our Moon altitude simulation scenario.

Figure 23 shows the effect of worsening the accuracy of the Doppler aiding from the orbital filter. It can be seen that with a 1-s update rate, Doppler accuracy of around 1 Hz (1σ) is required to maintain frequency tracking within the pull-in range of the FLL.

We also performed the same tests with the true Doppler errors produced by the orbital filter when operating the *WeakHEO* receiver in the Moon altitude scenario shown in Figure 17. Figure 24 shows the frequency tracking errors for five PRNs with realistic errors from the orbital filter. Here, the orbital filter aiding rate is every 10 s due to the output rate of the current *WeakHEO* platform. The frequency errors are generally maintained within the FLL pull-in range with a few excursions at 11 dB-Hz. This matches expectations from Figure 22, and further improvement would be anticipated with a one s update rate.

Aiding the receiver in this manner can allow it to track through dips and nulls in the transmit antenna pattern and therefore provide greater availability of satellites. More extensive testing with the orbital filter running in real time is planned to see if even weaker signals can be tracked and used for navigation. The use of data-less pilot channels should also be considered as these can remove squaring loss in the tracking

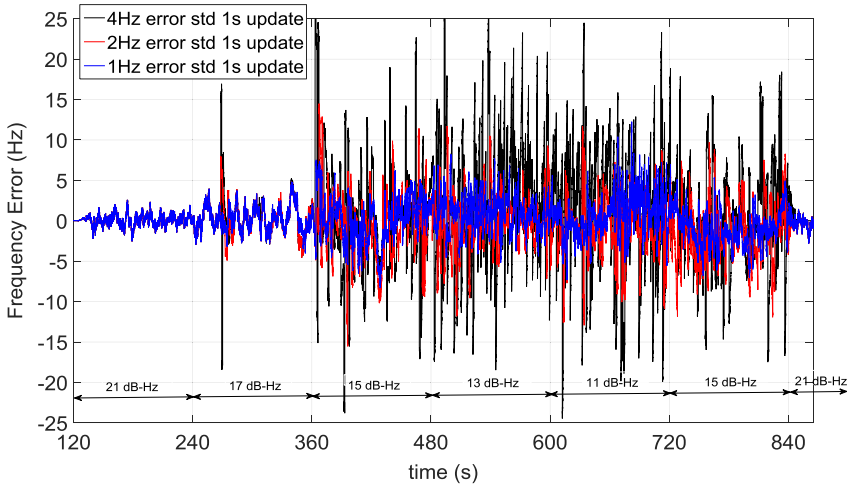

Fig. 23–Frequency errors of tracking PRN 26 with different aiding accuracies. [Color figure can be viewed at wileyonlinelibrary.com and www.ion.org]

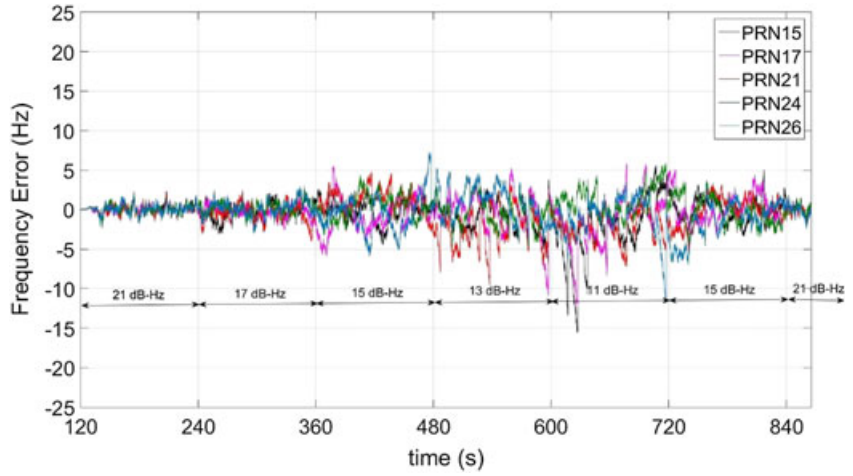

Fig. 24–Frequency errors of PRNs in the Moon altitude scenario aided by the orbital filter. [Color figure can be viewed at wileyonlinelibrary.com and www.ion.org]

and provide a wider pull-in range without the need for knowledge of the full navigation data bit sequence.

CONCLUSIONS

In this paper, following our previous studies, we first summarize the GPS signal characteristics in a lunar mission scenario. Then, we briefly describe a GPS L1 C/A receiver proof of concept and an adaptive orbital filter that processes the GPS observations, both designed in our lab, specifically for lunar missions. Finally, we describe in detail the benefit and the need of using the orbital filter kinematic estimation as aiding to the GPS signal processing module.

At Moon altitude, in order to compute a 3D position from GPS observations, the GPS receiver has to be capable of acquiring and tracking signals down to −168.5 dBm, affected by Doppler shifts and Doppler rates of up to 20 kHz and up to 3 Hz/s, therefore requiring a very high sensitivity architecture but also robust against high dynamics. Moreover, at the Moon altitude, GDOP higher than 1000 and ranging errors significantly higher than on Earth strongly reduce the achievable positioning accuracy that can be obtained through a single-epoch least-squares solution. An orbital filter is therefore considered.

The receiver uses GPS C/A code signals and utilizes full-bit length coherent integration throughout the acquisition, bit synchronization, and tracking. The orbital filter is an EKF, it uses a flexible orbital forces model (function of the altitude), and it adapts its covariance matrix of the measurements, when they are available, to the current estimated ranging errors in order to modify the filter gain accordingly, thus resulting in adaptive tuning. The simulation tests, carried out by processing realistic radio frequency signals generated by our Spirent GSS 8000 simulator for a highly elliptical MTO, show very promising acquisition and tracking sensitivities respectively of −169 dBm and −173 dBm (respectively 15 dB-Hz and 11 dB-Hz using Equation (9)) in high dynamics thanks to the orbital filter aiding, assuming an antenna gain of 10 dBi, and a positioning accuracy of a few hundred meters at Moon altitude. All stages can work autonomously or make use of the aiding from the orbital filter to provide greater sensitivity performance. However, the performance will be further improved in the next version of our receiver, "*WeakHEO 2*," where, thanks to larger hardware resources, the output rate of 0.1 Hz will be increased to 1 Hz and the limited number of 1 acquisition channel and 6 tracking channels will be enlarged as well. Furthermore, the orbital filter of the "*WeakHEO 2*" receiver will more efficiently filter directly the raw pseudorange and pseudorange rate observations instead of the single-epoch least-squares solution, allowing the filter to operate with less than four observations.

In a future step of the project, we will also consider tracking the other frequencies and signals of other GNSS constellations to further improve the navigation performance.

REFERENCES

1. Chiaradia, A. P. M., Gill, E., Montenbruck, O., Kuga, H. K., and Prado, A. F. B. A., "Algorithms for On-Board Orbit Determination using GPS OBODE-GPS," DLR - GSOC TN 00-04, 2000.
2. Choi, E. J., Yoon, Y. C., Lee, B. S., Park, S. Y., and Choi, K. H., "Onboard Orbit Determination using GPS Observations Based on the Unscented Kalman Filter," *Advances in Space Research,* Vol. 46, No. 11, 2010, pp. 1440–1451. https://www.ion.org/publications/abstract.cfm?articleID=11438.
3. Basile, G., Capuano, V., Botteron, C., and Farine, P.-A., "GPS Based Orbital Filter to Reach the Moon," *International Journal of Space Science and Engineering,* Vol. 3, No. 3, 2015, pp. 199–218.
4. Capuano, V., Basile, F., Botteron, C., and Farine, P.-A., "GNSS Based Orbital Filter for Earth Moon Transfer Orbits," *Journal of Navigation,* 2015, pp. 1–20.
5. Silva, P. F., Lopes, H. D., Peres, T. R., Silva, J. S., Ospina, J., Cichocki, F., Dovis, F., Musumeci, L., Serant, D., Calmettes, T., Pessina, I., and Perello, J. V., "Weak GNSS Signal Navigation to the Moon," *Proceedings of the 26th International Technical Meeting of the Satellite Division of The Institute of Navigation (ION GNSS+ 2013)*, Nashville, TN, September 2013, pp. 3357-3367.
6. Capuano, V., Botteron, C., Leclere, J., Tian, J., Yanguang, W., and Farine, P.-A., "Feasibility Study of GNSS as Navigation System to Reach the Moon," *Acta Astronautica,* Vol. 116, 2015, pp. 186–201.
7. Capuano, V., Blunt, P., Botteron, C., Tian, J., Leclere, J. W. Y., Basile, F., and Farine, P.-A., "Standalone GPS L1 C/A Receiver for Lunar Missions," *Sensors,* Vol. 16, No. 3, March 2016, pp. 347–368.
8. AGI, 10 November 2015. [Online], available: http://www.agi.com/products/stk/.
9. Capuano, V., Botteron, C., and Farine, P.-A., "GNSS Performances for MEO, GEO and HEO," *Proceedings of the 64th International Astronautical Congress*, Beijing, China, 2013.
10. Unwin, M., Van Steenwijk, R. D. V., Blunt, P., Hashida, Y., Kowaltschek, S., and Nowak, L., "Navigating Above the GPS Constellation – Preliminary Results from the SGR-GEO on GIOVE-A," *Proceedings of the 26th International Technical Meeting of the Satellite Division of The Institute of Navigation (ION GNSS+ 2013)*, Nashville, TN, September 2013, pp. 3305–3315.
11. Palmerini, G. B., Sabatini, M., and Perrotta, G., "En Route to the Moon using GNSS Signals," *Acta Astronautica,* Vol. 64, 2009, pp. 467–483.

12. Montenbruck, O. and Gill, E., *Satellite Orbits: Models, Methods, Applications,* Berlin, Germany, Springer, 2000.
13. Battin, R. H., *An Introduction to Mathematics and Methods of Astrodynamics*, AIAA Education Series, Reston, Virginia, 1968.
14. Basile, F., "Implementation of the Orbital Filter in a GNSS Receiver for Lunar Missions," University of Rome La Sapienza, École polytechnique fédérale de Lausanne (EPFL), Rome, Italy, 2015.
15. Groves, P. D., *Principles of GNSS, Inertial, and Multisensor Integrated Navigation Systems*, Artech House, Boston/London, 2013.
16. Martins, J. R. R. A., Sturdza, P., and Alonso, J. J., "The Complex-Step Derivative Approximation," *ACM Transactions on Mathematical Software,* Vol. 29, No. 3, 2003, pp. 245–262.
17. Lai, K. L. and Crassidis, J. L., "Generalizations of the Complex-Step Derivative Approximation," *AIAA Guidance, Navigation, and Control Conference and Exhibit,* 21–24 August, Keystone, Colorado, 2006. http://doi.org/10.2514/6.2006-6348.
18. "ICD-GPS-200F Navstar GPS Space Segment/User Segment Interfaces," 21 September 2011.
19. Kaplan, E. D. and Hegarty, C. J., *Understanding GPS: Principles and Applications*, Artech House, Boston/London, 2006.
20. van Diggelen, F., *A-GPS: Assisted GPS, GNSS and SBAS*, Artech House, Boston/London, 2009.
21. Musumeci, L., "Design of a Very High Sensitivity Acquisition," *Proceedings of IEEE/ION PLANS 2014*, Monterey, CA, May 2014, pp. 556–568.
22. Van Dierendonck, A. J., "GPS Receivers" in *Global Positioning System: Theory and Applications*, B. W. Parkinson and J. J. Spilker, Eds., Washington, D.C., AIAA, 1996.
23. Pany, T., *Navigation Signal Processing for GNSS Software Receivers*, Norwood, Artech House, 2010.